

# Lifetime Assessment for Thermal Barrier Coatings: Tests for Measuring Mixed Mode Delamination Toughness

Robert G. Hutchinson

Pratt & Whitney, MS 184-15, East Hartford, 06108 Connecticut

John W. Hutchinson<sup>†</sup>

School of Engineering and Applied Sciences, Harvard University, Cambridge, 02138 Massachusetts

**Mechanisms leading to degradation of the adherence of thermal barrier coatings (TBC) used in aircraft and power generating turbines are numerous and complex. To date, robust methods for the lifetime assessment of coatings have not emerged based on predictions of the degradation processes due to their complexity. In the absence of mechanism-based predictive models, direct measurement of coating adherence as a function of thermal exposure must be a component of any practical approach toward lifetime assessment. This paper outlines an approach to lifetime assessment of TBC that has taken shape in the past few years. Most TBC delaminations occur under a mix of mode I and mode II cracking conditions, with mode II delamination being particularly relevant. Direct measurement of TBC delamination toughness has been challenging, but recent progress has made this feasible. This paper surveys a range of potentially promising tests for measuring the mode dependence of delamination toughness with particular emphasis on toughness under mode II conditions.**

## I. Introduction

A thermal barrier coating (TBC) is a miracle of materials engineering and science that, aided by internal cooling, reduces the temperature on the underlying metal alloy substrate while withstanding repeated thermal cycles with variations on the order of 1000°C.<sup>1</sup> Research on the durability of TBCs has been underway since they were employed to extend the lifetime of turbine blades in aircraft engines roughly two decades ago. Efforts to improve TBC durability are driven by longevity considerations and also by the quest to achieve higher efficiency via higher operating temperatures.<sup>2</sup>

TBC systems generally involve three components: a metal bond coat with one surface adhering to the substrate alloy and the other surface oxidizing under thermal exposure to create an impervious aluminum oxide layer called the thermally grown oxide (TGO), and a porous ceramic topcoat which serves as the thermal insulation. Details of the coating failures depend on the specific materials making up the coating system. There are several bond coats in widespread use and these are typically in the range from 50 to 100  $\mu\text{m}$  thick. Most topcoats are yttria-stabilized zirconia. Depending on the application, the topcoat may be electron beam deposited with a columnar structure and typically on the order of 100  $\mu\text{m}$  thick (for aircraft engine blades) or plasma sprayed with a splat structure and as

thick as a millimeter or more (for hot surfaces in aircraft engines other than blades or most hot surfaces in gas power turbines).

Multiple failure modes leading to TBC spallation have been observed through laboratory tests and examination of coatings that have experienced service conditions. These observations have motivated extensive efforts to quantitatively characterize the micromechanics of the failure processes.<sup>3</sup> Many failures originate and propagate along the interface between the TGO and the bond coat (e.g., for some NiCoCrAlY bond coats) or just above the interface between the TGO and the topcoat (e.g., for some Pt–aluminide bond coats and for many plasma spray systems). Under conditions where the TBC is subject to very high temperature gradients through its thickness, failures have been observed to originate and propagate within the topcoat and well away from its interface with the TGO.<sup>4</sup> The focus in this paper will be on the most widely observed delamination failures that originate and propagate at the bottom of the topcoat, either just above or below the TGO.

While the micromechanical studies have provided considerable understanding of how delamination toughness degrades as a function of thermal history and while they have pointed to property changes that can lead to improvements in TBC systems, they are not yet sufficiently mature to allow quantitatively reliable prediction of delamination toughness degradation. This state of affairs is no different from essentially all other areas where fracture mechanics is used to assess structural integrity: fracture toughness is a property that is measured, not predicted, because models of toughness are usually not sufficiently accurate for prediction. Thus, the working assumption in this paper is that an essential component of any lifetime assessment scheme is the experimental determination of the delamination toughness of the TBC as a function of the relevant thermal history.

A fracture mechanics approach to TBC lifetime assessment that has emerged in recent years is introduced in the next section. Several of the most common delaminations will be reviewed illustrating that delamination usually occurs under mixed mode conditions. Mode II, or near-mode II, delaminations appear to be especially common. A modified four-point bend test<sup>5,6</sup> has proven to be an effective means of measuring delamination toughness under conditions with a nearly equal mix of mode I and II components. After a brief review of several tests for measuring delamination toughness, including the modified four-point bend test, the body of the paper surveys a range of possible tests to measure toughness over the full range of mode mix relevant to coating delaminations. Each of the proposed tests uses the modification used in the four-point bend test wherein a stiffener is bonded to the coating to increase the elastic energy available for delamination. If successfully implemented, the suite of tests has the potential to generate data over the range of mode dependence relevant to TBC delamination.

R. McMeeking—contributing editor

Manuscript No. 28891. Received November 11, 2010; approved February 11, 2011.

This paper is dedicated to the memory of A. G. Evans. His contributions form the foundations for much of the ongoing research on thermal barrier coatings.

<sup>†</sup>Author to whom correspondence should be addressed. e-mail: hutchinson@husm.harvard.edu

## II. Delamination Mechanics and Examples of TBC Delaminations

At temperatures representative of the highest temperatures experienced by coatings in service it is generally believed that stresses in the topcoat and the TGO are relaxed due to creep of the constituent materials. With this assumption, the largest in-plane stresses in the topcoat and TGO are compressive and they occur during cool down due to thermal expansion mismatch between the ceramic layers and the metal substrate. Thus, while the degradation processes primarily occur at high temperatures, it is generally believed that the critical conditions for delamination occur during cool down. The coatings must be able to withstand the stresses at the lowest temperatures when the turbines are cool. For this reason, the relevant toughness is believed to be “room temperature” toughness, and tests to measure the delamination toughness of TBC systems have invariably been conducted at room temperature.

A variety of simplified models are considered in this paper, none of which account for either the bond coat or the TGO. The model results presented here are intended to illustrate basic ideas; they will need to be embellished in quantitative applications to account for additional layers such as the TGO. In the models considered here, the Young's modulus and Poisson's ratio of the coating are,  $E_C$  and  $\nu_C$ , and those of the substrate are  $E$  and  $\nu$ . For plane strain, the two Dundurs elastic mismatch parameters are

$$\alpha = \frac{\bar{E} - \bar{E}_C}{\bar{E} + \bar{E}_C} \text{ and } \beta = \frac{1}{2} \frac{\mu(1 - 2\nu_C) - \mu_C(1 - 2\nu)}{\mu(1 - \nu_C) + \mu_C(1 - \nu)} \quad (1)$$

with  $\bar{E}_C = E_C/(1 - \nu_C^2)$ ,  $\bar{E} = E/(1 - \nu^2)$ ,  $\mu_C = E_C/[2(1 + \nu_C)]$  and  $\mu = E/[2(1 + \nu)]$ .

It is assumed that the interface plane is the weak link between the coating and the substrate and that the delamination crack stays within this plane. Kinking of an interface crack out of the interface region defeats the purpose of the test, and conditions that encourage the crack to stay within the interface will be discussed later in the paper. Denote the toughness of the controlling failure plane between the coating and the substrate (interface or interfacial layer) in its current state by  $\Gamma(\psi)$  in units  $J/m^2$  with the convention defined in Fig. 1 having the coating above the substrate. For most interfaces, the toughness depends on the mode mix as measured by  $\psi$  and as depicted in

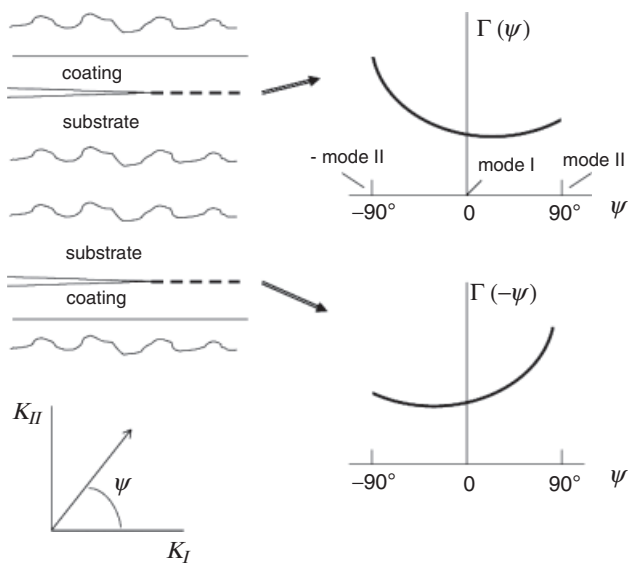


**Fig. 1.** Schematic of coating/substrate interface toughness as a function of mode mix. The convention in this paper defines the toughness function,  $\Gamma(\psi)$ , such that the coating lies above the substrate. When the coating lies below the substrate the toughness is  $\Gamma(-\psi)$  when subject to the mode mix,  $\psi$ . The toughness function  $\Gamma(\psi)$  can be symmetric in  $\psi$  but generally it should be assumed to be asymmetric.

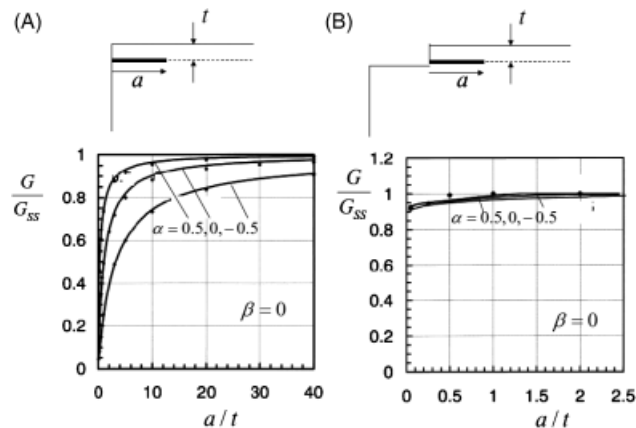


**Fig. 2.** Two examples of edge delamination cracks for a coating experiencing a tensile stress due to thermal expansion mismatch with the substrate. (A) An edge delamination emanating from an edge of the substrate. (B) An edge delamination emerging from a coating edge at an interior point of the substrate or possibly an open vertical sinter crack. For tensile stress, the crack is open with roughly equal components of mode I and mode II. For compressive stress, the crack is a mode II delamination, and the above results apply approximately if friction is neglected. The results reveal the inherently greater resistance to delamination initiation for coatings terminating at an edge compared with a coating terminating at an interior edge.

Fig. 1. If  $\beta = 0$ ,  $\psi = \tan^{-1}(K_{II}/K_I)$ , where  $K_I$  and  $K_{II}$  are the conventional mode I and II stress intensity factors. With the convention adopted in this paper (c.f., Fig. 1), the interface toughness for situations in which the coating lies below the substrate is  $\Gamma(-\psi)$ . The toughness function,  $\Gamma(\psi)$ , is not necessarily symmetric in  $\psi$  and, specifically, the negative mode II toughness,  $\Gamma(-90^\circ)$ , is not necessarily the same as the positive mode II toughness,  $\Gamma(90^\circ)$ . If  $\beta \neq 0$ , the definition of  $\psi$  is slightly more complicated and is given in Appendix A. With  $G$  as the energy release rate (units of  $J/m^2$ ) and  $\psi$  as the measure of the mode mix of the interface crack subject to the present loading, the condition for incipient advance of the delamination in the interface plane is

$$G = \Gamma(\psi) \quad (2)$$

The emphasis in this paper is on tests to measure  $\Gamma(\psi)$  for a wide range of  $\psi$  relevant to coating delamination failures.

Edge delaminations are among the most common TBC delaminations observed on components where spallations occur. Two types of edge delaminations are illustrated in Fig. 2. In these examples, the coating is taken to be of uniform thickness,  $t$ , and is bonded to an infinitely thick substrate. The film has a uniform thermal expansion mismatch with the substrate such that away from its edge the film is subject to a uniform equi-biaxial stress,  $\sigma$ . The steady-state, or long crack, energy release rate limit is independent of the delamination length:

$$G_{ss} = \frac{\sigma^2 t}{2E_C} \quad (3)$$

If the thermal mismatch conditions produce tensile stress in the coating, the crack is completely open with mix of mode I and II given by  $\psi \cong 55^\circ$ , depending somewhat on the elastic mismatch.<sup>7</sup> However, if the stress in the coating is compressive, as it would be for the TBC under cool down, the crack faces contact each other and the examples in Fig. 2 are *mode II (or near-mode II) delamination cracks* with  $\psi \cong -90^\circ$ .<sup>4</sup> Friction between the faces of the crack is neglected in these results.

<sup>4</sup>The results in Fig. 2 have been taken from Yu *et al.* [7] where a coating under tension due to a uniform thermal expansion mismatch is analyzed. The tensile loading produces an open crack. The results are only approximately valid for the compressive case due, in part, to neglect of contact that occurs between the crack faces. However, when friction is neglected, the energy release rate is only slightly affected by contact and the results in Fig. 2 are approximately applicable. An example where friction is taken into account in mode II delamination is considered later in this paper and a coating under compression is analyzed in Balint and Hutchinson.<sup>8</sup>

For an edge delamination emerging from an edge of the substrate in Fig. 2(A), the energy release rate,  $G$ , requires a delamination length,  $a$ , at least several times the coating thickness to approach the steady-state limit, even for a mismatch with  $\alpha = 0.5$  ( $\bar{E}_C/\bar{E} = 1/3$ ) which is representative of some TBC systems. By contrast, an edge delamination emanating from an interior edge of the coating as in Fig. 2(B) attains the steady-state limit when  $a$  is a small fraction of the coating thickness for all mismatches. An interior edge delamination arises, as illustrated, where the coating terminates abruptly away from the substrate edge or, for example, at an open vertical sinter crack in the coating. An interior coating edge is more susceptible to delamination initiation than a coating that extends all the way to the substrate edge. The latter has some built in protection against the initiation due to the extra compliance of the substrate edge that lowers the stress in the coating in that vicinity.

Edge delaminations can initiate from corners and from air holes in a substrate. As for delaminations emanating from a substrate edge, the local stress distribution in the coating will be affected by substrate compliance at such features. If the substrate thickness is comparable to that of the coating the compliance will be increased. A reduction in stored strain energy in the coating at potential initiation locations adds to the protection against delamination.

The mode mix of the delamination depends on the distribution of the compressive stress through the thickness of the coating. A uniform stress distribution, or a stress distribution which is more compressive at the surface than at the interface, produces mode II. If the stress is sufficiently more compressive just above the coating's interface than at its surface, then the crack may open.<sup>9</sup> For example, if the stress in the coating vanishes in a layer of thickness  $kt$  below the surface and is uniform compression in the remaining layer, then a mode I component will exist if  $k < 0.449$ ; otherwise mode II prevails. This example assumes no elastic mismatch between the coating and substrate, but elastic mismatch is less important than the details of the stress distribution.

### III. Tests for Measuring Delamination Toughness

Measuring the delamination toughness,  $\Gamma(\psi)$ , of TBC coatings has been challenging, especially so given the importance of a range of mixed mode toughness in applications. This section begins by citing several tests that have been used to measure delamination toughness and some representative results. The fracture mechanics approach to determining TBC durability is illustrated in conjunction with the tests.

Vastinonta and Beuth<sup>10</sup> used a conical brale C indenter to induce a circular delamination in a 100- $\mu\text{m}$ -thick electron beam deposited TBC system. The indenter is pushed into the substrate through the topcoat and TGO. The indenter forces an outward radial plastic flow of the substrate under the coating that decays with distance from the central axis of symmetry. The substrate motion induces additional compression of the coating in the radial direction and increases the elastic energy density stored in the TBC in the vicinity of the indent. The indenter also initiates a delamination edge where it pushes through the coating. The delamination spreads axisymmetrically until the driving force falls below the toughness, i.e., until  $G = \Gamma(\psi)$  can no longer be met. A difficult aspect of this test is the analysis of the delamination crack problem required to generate both  $G$  and  $\psi$  as a function of the radius delamination and the indenter depth. A sophisticated elastic-plastic finite element calculation is required. In addition, the induced radial compressive stress can be high enough to buckle the coating, further complicating the determination of  $G$  and  $\psi$ . The loading is a mix of mode I and mode II (with  $\psi > 0$  if buckling does not occur) that varies with crack radius.

Jones *et al.*<sup>11</sup> sliced a planar section of a electron beam deposited TBC system on a turbine blade substrate. Then these authors used a focused ion beam to cut a broad notch under the

coating system creating a trilayer bridge consisting of the bond coat, the TGO and the topcoat. The bridge was supported (effectively clamped) at its ends by the uncut substrate and coating system. A concentrated load normal to the surface was applied to the center of the bridge. In the first series of tests, the load was applied to the underside of the bridge pushing upward. This load produces a moment distribution in the bridge, which at sufficient force causes the topcoat to develop a vertical crack above the load that runs from the surface to the interface. This crack branches into the weak interface and spreads as a delamination crack. The geometry and preparation of the sample allow for clear visualization of the various stages, including the stable advance of the crack tip as the bridge is pushed upward. This is a highly sophisticated test that is not likely to be used routinely.

This in situ test allows for the interrogation of engine hardware but is a highly sophisticated test and is not likely to be used routinely. It also requires a detailed finite element analysis to obtain  $G$  and  $\psi$ . Plastic deformation of the metal bridge components can occur. The mode I component is somewhat larger than the mode II component when the load is applied under the bridge. To avoid cracking in brittle coatings and to obtain toughness data under conditions closer to mode II, Jones, Manning and Hemker (unpublished work) carried out a second set of tests in which they created a narrow open notch in the center of the top coat to the interface of interest and loaded the specimen by pushing down from above the bridge. This direction of loading adds to the compression in the coating from the thermal expansion mismatch and therefore more closely mimics the delamination conditions experienced in service. Kagawa and colleagues have developed two related tests, the barb test<sup>12</sup> and the push-out test,<sup>13</sup> to measure delamination toughness of TBCs. In each test, the coating is subject to additional compression by forcing it, but not the substrate, against a hard block. The force at which the coating delaminates is used to determine the critical energy release rate and the associated toughness. These tests add compression to any residual compression in the coating, but they impose a delamination displacement and shearing stress on the interface in the opposite direction from that experienced by a delamination in service driven by thermal expansion mismatch (i.e.,  $\psi > 0$  rather than  $\psi < 0$ ). The energy release rate and mode mix of the barb test has been analyzed by finite element methods<sup>14</sup> with the finding that  $\psi \cong 60^\circ$ . Like the aforementioned bridge test, the barb and push-out tests require highly refined specimen preparation and sophisticated testing which are likely to limit their use for routine toughness testing. Nevertheless, Kagawa and colleagues<sup>13</sup> have collected an extensive data set showing how the toughness

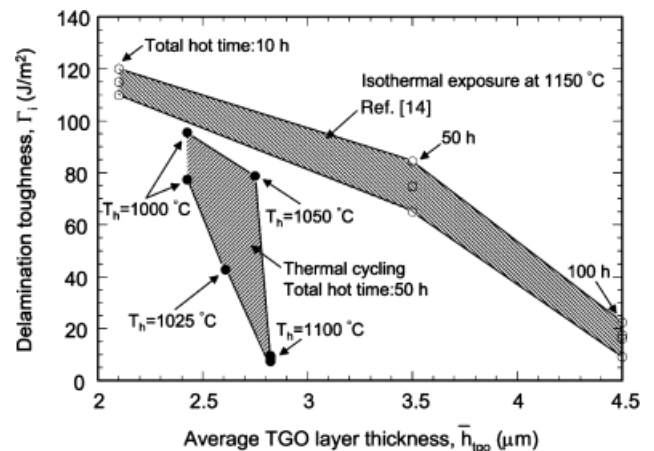
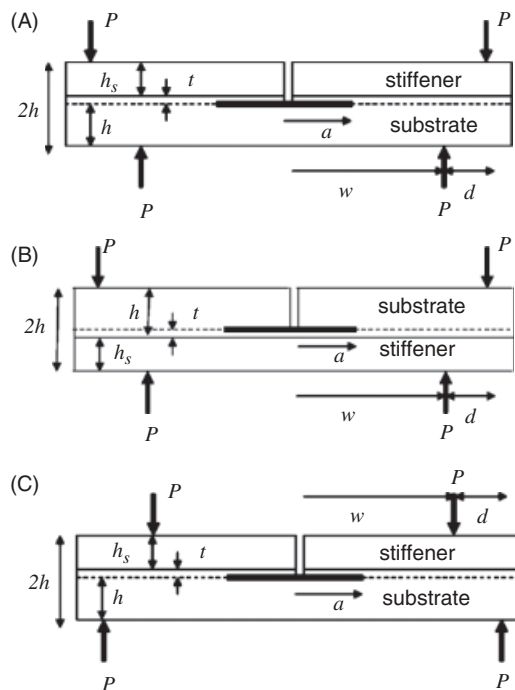


Fig. 3. Delamination toughness of an EB-PVD TBC on a NiCoCrAlY bond coat as a function of thermal exposure plotted as a function of the thickness of the TGO from Tanaka *et al.*<sup>15</sup> The upper band of data is for isothermal exposure and the lower band is for cyclic thermal exposure. The TGO thickness increases with thermal exposure time in accord with the markers on the upper band of data.



**Fig. 4.** Substrate/coating/stiffener trilayers. The coating thickness is  $t$ . The crack lies along the coating/substrate interface. (A) The four-point bend test with the loads configured to produce fully separated crack faces ( $\psi \cong 40^\circ$ ) giving  $\Gamma(\psi)$ . (B) The four-point bend test with the roles of the substrate and stiffener interchanged from that in (A) with  $\psi \cong 40^\circ$  giving  $\Gamma(-\psi)$ . (C) The inverted four-point test with the lines of action of the loading points interchanged or, equivalently, with specimen in (A) turned up-side down. The crack faces come into contact in the center of the specimen producing loading conditions with a larger component of mode II relative to mode I ( $\psi \cong -60^\circ$ ).

degrades with thermal exposure and with thermal cycling as illustrated in Fig. 3. The significant degradation of toughness with thermal exposure reflects the microcracking and other processes taking place at the delamination interface which lies either within the TGO or between the TGO and the bond coat, depending on the exposure time. Moreover, the toughness data for this system shows that thermal exposure under cycling is considerably more damaging than thermal exposure without cycling.

Generally, the popular four-point bend delamination test cannot be applied directly to measure the delamination toughness of coatings because the bending deformations required to create critical levels of stored energy in the coating become so large that extensive plastic deformation occurs in the substrate. To circumvent this difficulty, Hofinger *et al.*<sup>5</sup> proposed a modification of the four-point bend test wherein stiffeners are bonded to the surface of the coating with a gap cut at the center to allow delamination to occur (see Fig. 4(A) for an example). The loading bends the central section of the specimen upward so that when delamination occurs, the crack opens with a significant mode I component. The effectiveness of the test was demonstrated by measuring the delamination toughness of a plasma spray TBC coating.<sup>7</sup> The modified specimen enjoys the property of the conventional four-point bend test in that the delamination crack attains stable steady-state conditions when it is well within the central section between the inner loading points.<sup>15</sup> There are other advantages to the modified test. If the stiffener balances the substrate, the coating interface will lie near the neutral bending axis and, therefore, the bending load does not appreciably change the stress at the coating interface away from the crack tip. The energy for delamination is primarily provided by the elastic energy stored in the stiffener. In addition, if the coating is thin compared with the stiffener, most of the residual stress in the coating will not be released in the test because the coating remains bonded to the stiffener. Consequently, uncertainty in knowledge of the residual stress, which is

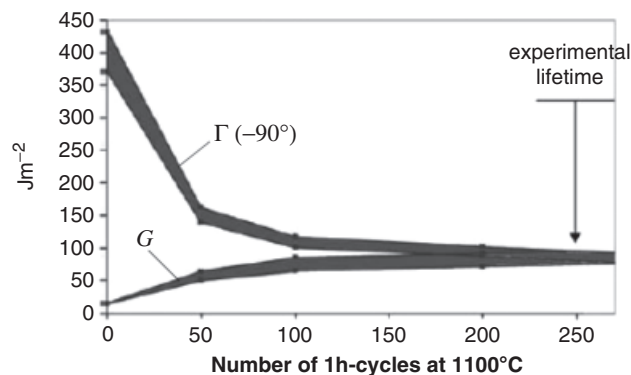


**Fig. 5.** A demonstration of the fracture mechanics approach for predicting TBC lifetime taken from Thery *et al.*<sup>6</sup> The system has a NiAlZr bond coat and a EB-PVD yttria-stabilized zirconia topcoat. The upper curve is the mode II toughness as a function of thermal cycles as inferred from four-point bend tests using a phenomenological conversion factor. The lower curve is the energy release rate predicted for a mode II edge delamination on the interface of the prototypical TBC system subject to the same thermal history.

common in many delamination tests, is not a serious disadvantage in the modified test because the residual stress makes very little contribution to either the energy release rate or the mode mix.

The modified four-point bend test was used by Thery *et al.*<sup>6</sup> at ONERA to conduct an extensive experimental study of the effect of thermal cycling on the delamination toughness of two TBC systems. The authors used this data in conjunction with estimates of the evolution of the energy release rate,  $G$ , for a prototypical demonstration of the efficacy of the fracture mechanics approach to delamination based on the fracture condition (2). The demonstration for one of the TBC systems considered by the ONERA group is reproduced in Fig. 5. One complication the authors faced was that the measured value of the toughness in their modified bend test corresponds to a mixed mode with  $\psi \cong 40^\circ$  while the toughness relevant to their prototypical test (which involved edge delamination) was close to pure mode II with  $\psi \cong -90^\circ$ . The mode II toughness plotted in Fig. 5 was converted from the measured toughness using a phenomenological amplification factor,  $\cong 3.7$ , to account for the higher toughness in mode II, together with an implicit assumption that the toughness is not strongly dependent on the sign of  $\psi$ .<sup>6</sup> The degradation of toughness with thermal cycles seen in Fig. 5 is qualitatively similar to that displayed in Fig. 3. The increase in  $G$  with thermal cycles is due to the increase in stored residual elastic energy upon cool-down associated with the increases in the thickness of the TGO and modulus of the topcoat. Failure of the TBC in the prototypical demonstration was in reasonable agreement with attainment of condition (1) for both TBC systems in the study. The fact that the mode II toughness estimate used to obtain this agreement is so much higher than the toughness measured in their four-point bend test (with  $\psi \cong 40^\circ$ ) highlights the significance of mode dependence.

#### IV. Potential Tests for a Full Range of Mixed Mode Delamination Toughness

In this section, a selection of basic tests is reviewed in order to determine whether one or more may prove to be an effective means of generating delamination toughness data for TBCs and other coating systems. To focus attention on the most important details of the tests, consideration will be confined to specimens of type shown in Fig. 4 where the modulus and Poisson's ratio of the stiffeners will be taken to be identical to that of the substrate,  $E$  and  $\nu$ . The bond coat is considered to be part of the substrate and the TGO is not explicitly considered. The coating has thickness  $t$  and modulus and Poisson's ratio,  $E_C$  and  $\nu_C$ . The

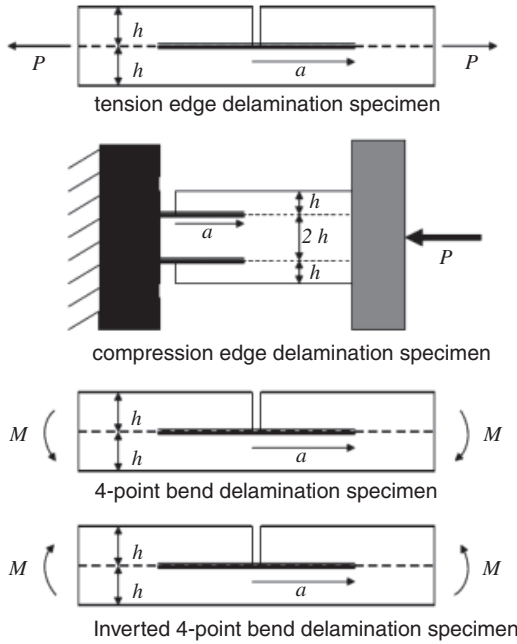


**Fig. 6.** Basic specimens for measuring different modes of delamination toughness. These specimens are shown without any coating.

thickness of the stiffeners is  $h_s$  and, to focus just on the essential details, it will be assumed that this thickness has been chosen such that the bending stiffness of the coating/stiffener bilayer,  $B$ , is the same as that of the substrate layer, i.e.,  $B = \bar{E}h^3/12$ . Thus, the neutral axis of the modified specimen under pure bending lies approximately along the interface between the coating and the substrate. As in the case of the modified four-point bend test, the purpose of the stiffener is to substantially boost the stored elastic energy available to drive the delamination. In fact, for specimens such as those in Fig. 6 subject to tension or compression, the stiffener is even more effective in storing energy than for the bend-type specimens.

It has been remarked that only a small fraction of the residual stress in the coating is released to drive delamination if the coating is thin and/or compliant compared with the stiffener. Under these circumstances the delaminated coating is constrained assuming it remains bonded to the stiffener. Suppose the coating has a uniform stress,  $\sigma$ , before bonding the stiffener. The fraction of the elastic energy in the coating that is released when the coating/stiffener bilayer is separated from the substrate is readily

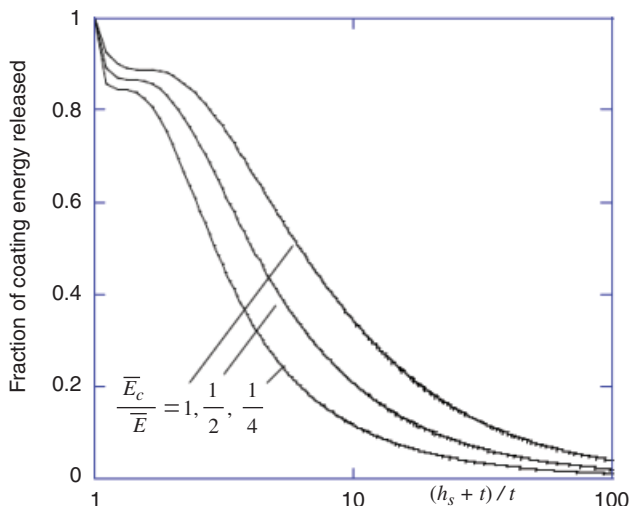


**Fig. 7.** The fraction of elastic energy stored in the coating that is released to delaminate a coating/stiffener bilayer from the substrate. The stress in the coating before delamination is assumed to be uniform.

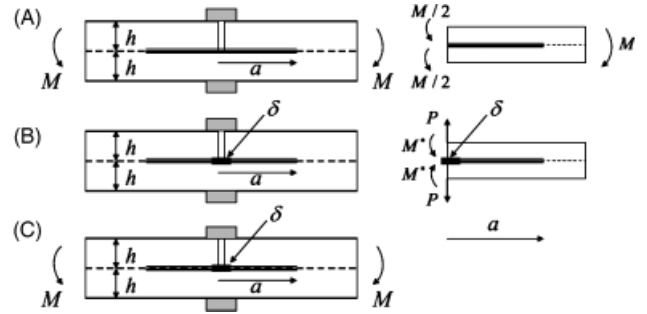


**Fig. 8.** (A) Mode II bend test (positive or negative  $M$ ) constrained such that the upper layer does not rotate at the center but is free to slide laterally without friction. (B) Mode I wedge test constrained such that layers do not rotate at the center ( $M^* = Pa/2$ ). (C) Mixed mode test under combined frictionless bending and wedging and constrained against rotation at the center. These specimens are shown without any coating.

calculated. The released fraction is the difference between the initial strain energy in the coating and the strain energy in the coating/stiffener bilayer after separation. The released fraction is plotted in Fig. 7 for combinations of  $(h_s+t)/t$  and  $\bar{E}_C/\bar{E}$ . This plot can be used to assess if it is possible to ignore the role of the residual stress in the coating in the modified tests. If residual stress cannot be ignored, then Fig. 7 can be used to estimate the contribution from the residual stress to  $G$  assuming the residual stress is known. It is important to note that, while the residual stress contribution can be added to the contributions to  $G$  from the applied load, the phase angle,  $\psi$ , characterizing the mode mix must be computed by a linear superposition of the mode I and II stress intensity factors from the two contributions.

We begin by giving basic mechanics results for  $G$  and  $\psi$  for a number of potential specimens for the case where the coating is absent or, equivalently, with  $E_C = E$ . The loading cases are presented and labeled in Figs. 6, 8, and 9. The simple formulas presented in this section all apply under conditions when the crack length,  $a$ , exceeds several times the layer thickness,  $h$ , and has not yet begun to interact with the load points or with the ends of the specimen. Finite element results for some of the specimens will be used to demonstrate the validity of the basic results and to clarify issues related to crack face contact and friction. Following presentation of results for the homogeneous specimens, the mode mix  $\psi$  in the presence of the coating will be addressed.

**(1) Homogeneous Specimens with no Coating Layer**

For the specimens in Fig. 6:

*Tension edge delamination specimen :*  

$$G = \frac{\sigma^2 h}{E}, \quad \psi = 49.1^\circ \quad (\sigma = P/2h) \tag{4}$$

*Compression edge delamination specimen :*  

$$G = \frac{\sigma^2 h}{E}, \quad \psi = -90^\circ \quad (\sigma = -P/4h) \tag{5}$$

*Four-point bend specimen :*  

$$G = \frac{7}{16} \frac{M^2}{B} = \frac{21}{4} \frac{M^2}{\bar{E}h^3}, \quad \psi = 40.9^\circ \tag{6}$$

*Inverted four-point bend specimen :*  

$$G = \frac{1}{4} \frac{M^2}{B} = 3 \frac{M^2}{\bar{E}h^3}, \quad \psi = -60^\circ \tag{7}$$

In each of these examples, the energy release rate and the mode mix are steady-state values, which are independent of crack length. For long cracks in long specimens in Fig. 6, (4) and (6) are results from exact two dimensional elasticity solutions<sup>9</sup> while (7) is the result of a beam analysis presented in Appendix

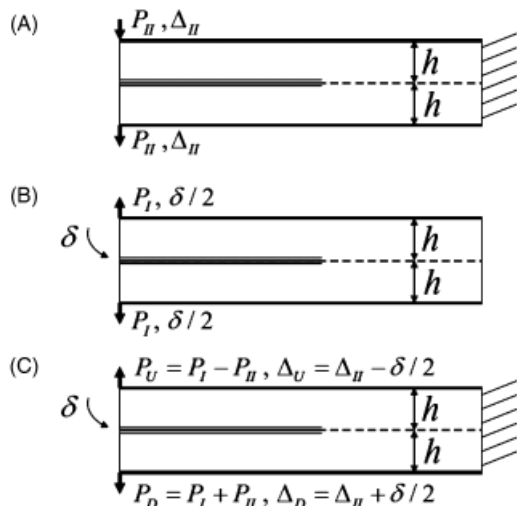


Fig. 9. (A) Mode II end-loaded double-cantilever beam. (B) Mode I wedge-loaded double-cantilever beam. (C) Mixed mode double-cantilever beam as superposition of (A) and (B).

A. Friction is neglected for the compression edge-delamination specimen in (5) but is considered in numerical simulations presented below. The energy release rate (5) is derived assuming that the two cracks in the specimen grow together maintaining symmetry. This will not necessarily occur and the possibility of growth of just one of the cracks should also be considered. Specimen dimensions needed to preclude elastic buckling and plastic deformation of the compression specimen are readily established and easily met. Elastic buckling is precluded if  $L/h < (\bar{E}h/\Gamma)^{1/4}/(2\pi\sqrt{3})$ , while avoidance of plastic deformation requires  $h > \bar{E}\Gamma/\sigma_y^2$ , with  $\Gamma$  as the mode II toughness.

Contact between the crack faces occurs in the center of the inverted four-point bend specimen at the free ends of the upper layers; friction is neglected in (7). The accuracy of (7) for the inverted bend specimen is confirmed by finite element simulations presented in Fig. 10. The ANSYS code has been used in the calculations and the contact option has been invoked to account for crack face contact. In contact regions, Coulomb friction is invoked with a friction coefficient,  $\mu_f$ . For the friction cases, the results apply for monotonically increasing  $M$  with fixed crack length. Details of the finite element modeling are

given in Appendix A. For the frictionless case, steady-state conditions (7) are attained when the crack length exceeds about  $2h$ , and for crack lengths below  $2h$  the energy release rate is below the steady-state limit and the mode mix emerges from negative mode II ( $\psi = -90^\circ$ ). Friction lowers the energy release rate, but decreasingly so as the crack gets longer because the normal contact force diminishes. The mode mix is relatively unaffected by friction. It should be possible to reduce friction at the single point of contact by lubrication with a thin film of low friction material.

The compression edge-delamination specimen in Fig. 6 would appear to provide a relatively straightforward test for measuring mode II toughness relevant to edge delaminations, although there are complications that have to be addressed related to crack face contact, friction, and symmetric crack growth. Selected finite element simulations have been carried out to gain preliminary insights into some of these effects. The applied load,  $P = -4\sigma h$ , is increased monotonically such that for any fixed crack length,  $a$ , the stresses throughout the specimen increase linearly with  $\sigma$ , the mode mix is constant, and the energy release rate and the work dissipated in friction increase in proportion to  $\sigma^2$ .

For the frictionless limit, Fig. 11(A) displays the normalized pressure,  $p/\sigma$ , along the crack faces for three values of fixed  $a/h$ , while Fig. 11(B) presents the opening gap,  $\delta$ , between the faces. Crack face contact occurs in the vicinity of the crack tip in all cases and thus the crack is mode II with  $\psi = -90^\circ$ . The shortest crack with  $a/h = 0.4$  is closed over its entire length and has high pressure between the faces at the end of the contact region ( $x/a = 1$ ). The two longer cracks are effectively open at distances greater than about  $2h$  from the tip. The peak pressure between the faces for the long cracks occurs at a distance of roughly  $h/2$  from the tip. In the finite element model the crack in the right half of the specimen has length  $a$  originating from a notch at the center of the upper layer with half-width  $h/10$ .

The energy release rate and mode II stress intensity factor of the compression edge-delamination specimen are plotted as a function of the crack length in Fig. 12 for the frictionless case and for two values of the friction coefficient. Steady-state conditions are attained at crack lengths greater than about  $h$  for both the frictionless case (with  $G = G_{SS}$  given by (5)) and the two cases with Coulomb friction. Friction clearly influences the energy release rate, but the effect is relatively modest for these examples. The reason that a steady state exists for the frictional cases is due to the fact that the contact region is confined to a

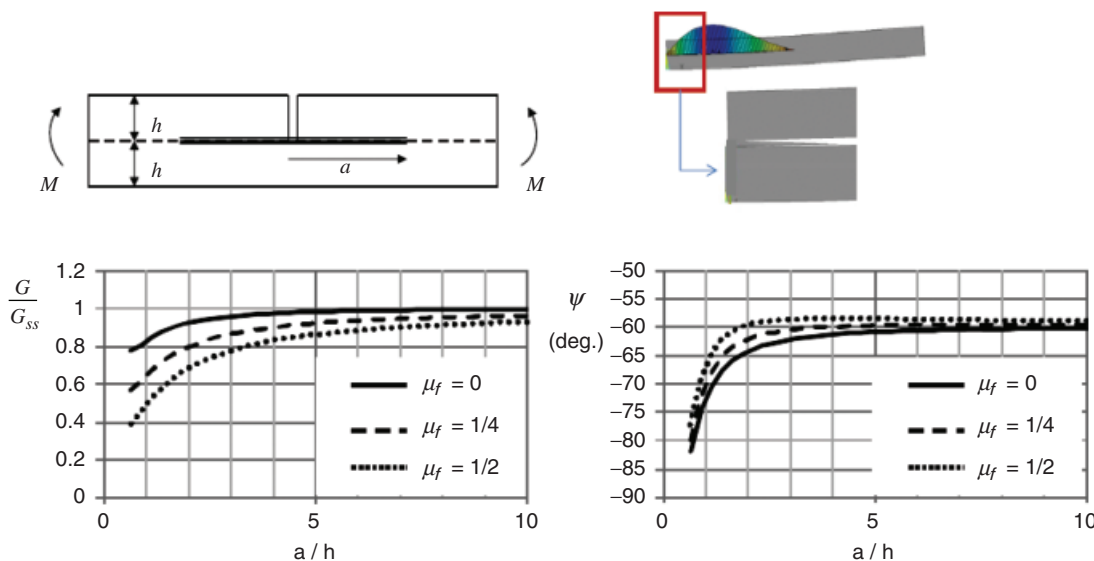


Fig. 10. Finite element results for  $G$  and  $\psi$  for the inverted four-point bend specimen in Fig. 6. The steady-state energy release rate for the frictionless limit ( $\mu_f = 0$ ),  $G_{SS}$ , is given by (7) and derived in Appendix A based on beam analysis. This same analysis gives  $\psi = -60^\circ$ . Results for the two cases with Coulomb friction have been computed under monotonically increasing  $M$  with  $a/h$  fixed. The analysis verifies that the crack is open except for a small contact region at the center of the specimen.

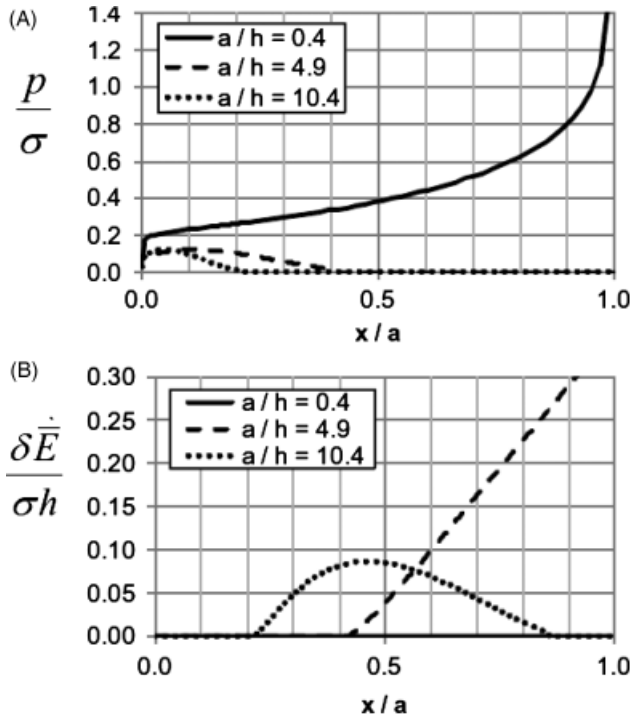


Fig. 11. (A) Normalized pressure between crack faces in the regions of contact, and (B) normalized gap between the faces in the regions where no contact occurs. These are for the compression edge-delamination specimen in Fig. 6 with no friction for three values of normalized crack length  $a/h$ . The coordinate  $x$  is measured from the crack tip along the crack faces. Friction makes only modest changes to the region of contact.

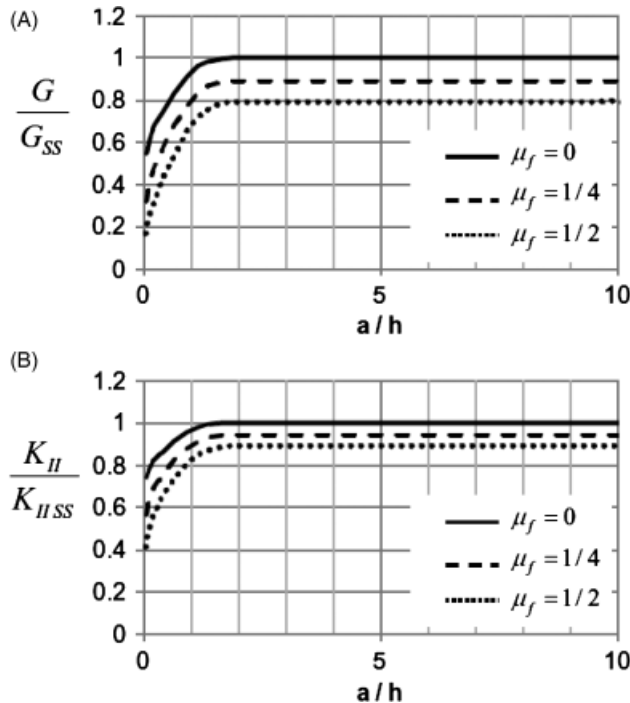


Fig. 12. (A) Normalized energy release rate and (B) normalized mode II stress intensity factor as a function of crack length for the compression edge-delamination specimen in Fig. 6 under monotonically increasing applied load for the frictionless case and two values of Coulomb friction. The steady state energy release rate,  $G_{SS} = \sigma^2 h / \bar{E}$ , and the steady state mode II stress intensity factor,  $K_{II,SS} = \sigma \sqrt{h}$ , for the frictionless case have been used in the normalizations.

zone of width about  $2h$  behind the tip. Thus, for a given friction coefficient, all long cracks have essentially the same zone of frictional sliding behind the tip dissipating the same amount of energy. The dissipation scales with  $\sigma^2$  but is not strictly linear in  $\mu_f$ . Under certain circumstances, it is possible that this frictional dissipation may be included as part of the fracture process energy forming the mode II toughness.<sup>8</sup> Further study of crack face contact and frictional sliding on the compression edge-delamination specimen is clearly required before it can be used to extract mode II delamination toughness. Nevertheless, the results presented in Figs. 11 and 12 are promising in the sense they suggest that it may be possible to obtain relatively simple characterizations of the specimen.

In principle, the *constrained bend-wedge mixed mode specimen* and loadings in Fig. 8(C) allow access to the entire range of mixed mode loading. It is imagined that a specially designed fixture, or guide, has been inserted at the center of the specimen such that the end of the coating-stiffener bilayer is constrained against rotation but is free to slide without friction relative to the substrate layer. This fixture is also assumed to be capable of forcing a separation,  $\delta$ , of the crack faces at the center of the specimen.

*Mode II constrained bend test* (Fig. 8(A)):

$$K_I = 0, \quad K_{II} = \frac{3}{2} M h^{-3/2}, \quad G = \frac{3}{16} \frac{M^2}{B} \quad (8)$$

*Mode I constrained wedge test* (Fig. 8(B)):

$$K_I = \sqrt{3} P a h^{-3/2}, \quad K_{II} = 0, \quad G = \frac{1}{4} \frac{P^2 a^2}{B} \quad (9)$$

These results have been determined using a beam theory analysis; (8) is exact plane strain elasticity for a long crack. The result in (9) is approximate but increasingly accurate for long cracks. For intermediate length cracks, its accuracy can be improved by the inclusion of an extra term depending on  $a/h$ .<sup>16</sup>

The *constrained bend-wedge mixed mode test* in Fig. 8(C) is obtained from the linear superposition of (8) and (9):

$$G = \frac{3}{16} \frac{M^2}{B} + \frac{1}{4} \frac{P^2 a^2}{B}, \quad \tan \psi = \frac{\sqrt{3} M}{2 P a} \quad (10)$$

The crack faces will be open if  $P > 0$  and the full range of  $\psi$  is accessed by reversing the sign of  $M$ . Crack growth is usually unstable if  $P$  is prescribed, but not if the opening displacement  $\delta = P a^3 / 6 B$  is prescribed. With  $\Theta$  as the rotation through which the moment  $M$  at the right end of the specimen works, beam theory gives:  $\Theta = (w + a) M / 8 B$  where  $w$  is the distance from the center to the right end of the specimen. The results in (10) can be rewritten as

$$G = 12 \frac{B \Theta^2}{(w + a)^2} + 9 \frac{B \delta^2}{a^4}, \quad \tan \psi = \frac{2 \Theta a^2}{\sqrt{3} \delta (w + a)} \quad (11)$$

The energy release rate decreases under prescribed rotation and opening displacement and crack growth will usually be stable. For example, if an opening,  $\delta$ , is prescribed and held fixed while  $\Theta$  is increased from zero, the mode mix will increase from pure mode I toward mode II. If the crack length can be measured, the results in (11) suggest a means of measuring the interface toughness over the entire range of  $\psi$ .

Various loadings of a *double-cantilever beam specimen* are depicted in Fig. 9. The *mode II double-cantilever beam specimen* in Fig. 9(A) has

$$K_I = 0, \quad K_{II} = 3 P_{II} a h^{-3/2}, \quad G = \frac{3}{4} \frac{P_{II}^2 a^2}{B} \quad (12)$$

The mode I double-cantilever beam specimen in Fig. 9(B) has

$$K_I = 2\sqrt{3}P_I a h^{-3/2}, \quad K_{II} = 0, \quad G = \frac{P_I^2 a^2}{B} \quad (13)$$

Superposition of the above gives for the mixed mode double-cantilever beam specimen

$$G = \frac{P_I^2 a^2}{B} + \frac{3}{4} \frac{P_{II}^2 a^2}{B}, \quad \tan \psi = \frac{\sqrt{3}P_{II}}{2P_I} \quad (14)$$

The accuracy of both contributions to  $G$  can be improved by including extra terms of order  $h/a$ , as has been done in Hutchinson and Suo.<sup>9</sup> Based on beam theory predictions,  $\Delta_{II} = P_{II}(w^3 + 3a^3)/12B$  and  $\delta = 2P_I a^3/3B$ , such that one can rewrite (14) as

$$G = 108 \frac{B\Delta_{II}^2 a^2}{(w^3 + 3a^3)^2} + \frac{9}{4} \frac{B\delta^2}{a^4}, \quad (15)$$

$$\tan \psi = \frac{4\sqrt{3}a^3 \Delta_{II}}{(w^3 + 3a^3)\delta}$$

The crack will be open if  $\delta > 0$  and crack growth is expected to be stable under prescribed displacements.

In the literature of laminated composites, double-cantilever specimens are also called end-notched specimens and they have been widely used to the measure mixed mode toughness dependence with various loadings including those outlined above. An important recent development is a loading device for carrying out a mixed mode double-cantilever test by applying unequal moments to the two layers.<sup>17</sup> This system is capable of applying the full range of mode mix and it has the advantage that steady-state crack growth occurs under constant applied moments. This system holds great promise for TBC testing if it could be scaled down to an appropriate size.

The *Brazil nut specimen* has been used successfully to measure a substantial range of mixed mode toughness for specific interfaces<sup>18</sup> and for composite laminates.<sup>19</sup> It is possible this specimen could also be adapted to measure TBC coating delamination toughness by bonding one half of a circular metallic disk to the surface of the coating and the other half to the underside of the substrate. Unlike the test just described, the Brazil nut test does not exhibit a steady-state and crack growth can occur unstably. The range of energy release rates achievable in the Brazil nut test with a specimen having a radius on the order of 1 cm is sufficient to drive most coating delaminations. Friction is also a concern in this test.<sup>20</sup>

## (2) Specimens with a Coating Layer

For all of the tests discussed above, the effect of the elastic mismatch of the coating layer on the mode mix of the interface crack can be estimated simply if the coating is thin compared with the thickness of the substrate and the stiffener. The delamination crack lies on the interface between the coating and the substrate. An important distinction is whether the coating lies above or below the substrate, as has been noted in Fig. 1. With the convention employed in this paper, the interface toughness for a coating lying above the interface is  $\Gamma(\psi)$ , while that for a coating lying below the interface is  $\Gamma(-\psi)$ . As in the previous section, the discussion which follows assumes that the bending stiffness of the coating/stiffener bilayer,  $B$ , is the same as that of the lower substrate layer,  $\bar{E}h^3/12$ . With this choice, all of the above expressions for the energy release rate are the same, to the accuracy to which they hold.<sup>8</sup> It will also be assumed that the

<sup>8</sup>Some of the energy release rates may vary slightly from those quoted if one undertook more accurate plane strain calculations. It is strongly recommended that finite element calculations of final specimen geometries and properties be performed. Such calculations also reveal when the crack begins to interact with the specimen ends. In this paper, to simplify the discussion, we have taken the bending stiffness of the bilayer to be the same as that of the lower layer, and we have not directly accounted for the TGO. These effects, and contributions from residual stress in the coating, can be included if one is prepared to compute the energy release rate and the mode mix for the specimen.

**Table I. The Phase Angle Shift,  $\omega(\alpha, \beta)$  in Degrees, for Combinations of the Elastic Mismatch Parameters<sup>21</sup>**

$\beta$	$\alpha$								
	-0.8	-0.6	-0.4	-0.2	0.0	0.2	0.4	0.6	0.8
-0.4	2.2	3.5							
-0.3	3.0	4.0	3.3	1.4					
-0.2	3.6	4.1	3.4	2.0	-0.3	-3.3			
-0.1	4.0	4.1	3.3	2.0	0.1	-2.3	-5.5	-10.8	
0.0	4.4	3.8	2.9	1.6	0.0	-2.1	-4.7	-8.4	-14.3
0.1			2.3	1.1	-0.5	-2.3	-4.5	-7.4	-11.6
0.2					-1.3	-3.0	-4.9	-7.3	-10.5
0.3							-5.8	-7.8	-10.4
0.4									-11.1

coating is sufficiently thin and/or compliant that the elastic energy released associated with the residual stress in the coating can be ignored, as discussed in conjunction with Fig. 7.

The mode mix for the crack on the interface between the coating and the substrate, as measured by  $\psi$ , can be estimated using a general asymptotic relationship for cases with  $t/h \ll 1$ .<sup>21</sup> Denote the mode mix for any of the specimens in the absence of a coating (i.e., with  $t=0$ , or, equivalently, with  $E_C = E$  and  $\nu_C = \nu$ ) by  $\psi^0$ , and denote the mode mix for the crack on the interface between the coating and the substrate under the same loading by  $\psi$ . The relation between the two measures is

$$\psi = \psi^0 \pm \omega(\alpha, \beta) \quad (16)$$

where the “+” applies if the coating lies below the substrate and the “-” applies if the coating lies above the substrate and where  $\omega(\alpha, \beta)$  is given in Table I.<sup>†</sup> For thin coatings ( $t/h \ll 1$ ), this asymptotic result does not depend on  $t$ . The result (16) is based on an elasticity analysis of a crack on a bimaterial interface which, for  $\beta \neq 0$ , neglects the consequences of crack face interpenetration behind the crack tip on the assumption that the interpenetration is subsumed within the fracture process zone. Thus, (16) is limited to cases in which interpenetration does not invalidate application of the solution. If  $\beta \neq 0$ , the predicted zone of interpenetration increases as the loading becomes dominantly mode II, and thus (16) should be used with caution near mode II.

To illustrate the effect of elastic mismatch between the coating and the substrate for the specimens in Fig. 6, suppose  $\bar{E}_C/\bar{E} = 1/4$  and  $\nu_C = \nu = 0.3$ : then,  $\alpha = 3/5$ ,  $\beta = 0.17$  and, from Table I,  $\omega = -7.3^\circ$ . If the coating lies above the substrate, by (16), phase angle of the *tension edge-delamination specimen* increases from  $\psi^0 = 49.1^\circ$  to  $\psi = 56.4^\circ$ ; that of the *four-point bend specimen* increases from  $\psi^0 = 40.9^\circ$  to  $\psi = 48.2^\circ$ ; while mode II component of the *inverted four-point bend specimen* decreases by  $\psi^0 = -60^\circ$  to  $\psi = -52.7^\circ$ . The mode II component of the compression edge-delamination specimen is also predicted to decrease from  $\psi^0 = -90^\circ$  to  $\psi = -82.7^\circ$ , but this should only be considered as a trend rather than a quantitative estimate for reasons mentioned above. In general, the shift in mode mix due to the compliance of the coating layer is relatively small, as these results illustrate, except for coatings that are exceptionally stiff or compliant.

## (3) Interchanging the Substrate and Stiffener

For any of the specimens considered, by turning the trilayer upside down and creating a notch down to the interface in the substrate and having a single continuous stiffener, one can access  $\Gamma(\psi)$  in the opposite sign range of  $\psi$ . The interchange in Fig. 4 from (A) to (B) illustrates precisely what this entails. The

<sup>†</sup>This table is reproduced from Suo and Hutchinson.<sup>21</sup> In Suo and Hutchinson,<sup>21</sup> the thin layer was taken to lie below substrate and thus “+” was used. Here, the convention of the earlier reference in defining the Dundurs parameter was followed wherein  $\alpha > 0$  for systems with coatings more compliant than substrates. The reader should be alert to the fact that the usual convention has  $\alpha > 0$  when the material above the interface crack is stiffer than the material below it.

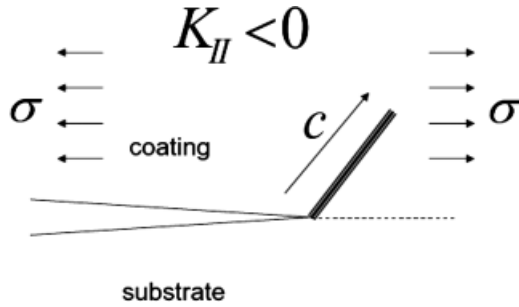


**Fig. 13.** Conventions related to kinking of an interface crack into the coating. For a coating lying above the substrate, as shown, a negative  $K_{II}$  encourages kinking into the coating. If the coating lies below the substrate a positive  $K_{II}$  encourages kinking into the coating. A tensile residual stress in the coating ( $\sigma > 0$ ) increases the likelihood of kinking into the coating while a compressive residual stress ( $\sigma < 0$ ) discourages kinking into the coating.

discussion, which follows continues to assume the interface of interest is that between the substrate and the coating. As noted in Fig. 1, inverting the substrate/coating bilayer changes the toughness from  $\Gamma(\psi)$  to  $\Gamma(-\psi)$  if the mode mix on the interface does not change. Let  $\psi^0$  be the reference mode mix of the specimen under the particular loading in the absence of the coating as defined above. If the coating lies above the substrate (as in Fig. 4(A)), then  $\psi = \psi^0 - \omega$  and the toughness is  $\Gamma(\psi^0 - \omega)$ . If the coating lies below the substrate (as in Fig. 4(B)), then  $\psi = \psi^0 + \omega$  and the toughness is  $\Gamma(-\psi^0 - \omega)$ .

The possibility of interchanging the roles of the substrate and the stiffener in this manner has several advantages. The most obvious advantage is that it potentially provides a method to generate data for both positive and negative mode II contributions. Less obvious is the advantage that can accrue by changing the position of the coating relative to the substrate in helping to suppress kinking of the crack out of the interface. As discussed in the next subsection, the sign of the mode II stress intensity factor and the location of the coating relative to the interface can have a strong influence on the propensity of the crack to remain in the interface, especially if the interface toughness is comparable to that of the coating. Thus, a delamination crack that tends to stray from the interface for one substrate/coating/stiffener configuration might remain in the interface when the roles of the substrate and stiffener are interchanged in the manner suggested. In other words, if it is difficult to measure  $\Gamma(\psi)$  for loadings with one sign of  $\psi$ , it may be possible to measure the toughness for the opposite sign of  $\psi$ . For toughness functions, which are symmetric in  $\psi$ , this would suffice. Generally, however,  $\Gamma(\psi)$  need not be symmetric in  $\psi$ , as the set of data for an epoxy/glass interface illustrates.<sup>22</sup> For some interfaces  $\Gamma(\psi)$  does appear to be symmetric.<sup>19</sup>

#### (4) Propensity for a Delamination Crack to Remain in or Near the Interface

Success in measuring delamination toughness requires that the path followed by the crack in a test is similar to the path followed by the crack in the application of interest. If the interface between the coating and the substrate has low toughness compared with the coating itself (and compared with the substrate, which for the discussion here will be assumed to be very tough), then crack propagation initiated in the interface is likely to remain in the interface for all loading conditions. Depending on the actual system, this interface might lie between the coating and the TGO or between the TGO and the bond coat. For systems without a TGO, this interface would lie between the coating and the bond coat. For some coating systems, delaminations occur within the coating but just above the coating/substrate interface (i.e., just above the TGO if one is present or above the bond coat if not). This may be a consequence of loading conditions which continually drive the crack toward the interface, as

discussed below, or it may be due to the existence of a very thin interfacial layer of less tough material. Residual stress in the coating can also play a role in determining whether the crack stays in or near the interface. A residual compressive stress in the coating acts to discourage cracks from turning into the coating, while tensile stress encourages deviations away from the interface or the low-toughness interfacial layer. A few brief observations related to these effects close out this section.

With the coating above the substrate and with the tip at the right end of the interface crack as in Fig. 13, a positive  $K_{II}$  ( $\psi > 0$ ) would promote kinking of the crack downward into the substrate were it not too tough. Thus, if a crack is propagating in the coating just above the interface, a positive  $K_{II}$  will tend to cause it to hug the interface. Conversely, a negative  $K_{II}$  ( $\psi < 0$ ) promotes upward kinking into the coating. If the coating lies below the interface the situation reverses: a positive  $K_{II}$  ( $\psi > 0$ ) promotes downward kinking into the coatings while a negative  $K_{II}$  ( $\psi < 0$ ) keeps the crack in or near the interface. Quantitative conditions based on the relative toughness of the interface to that of the coating are available for assessing the likelihood of kinking out of the interface when the sign of  $K_{II}$  promotes kinking into the substrate.<sup>23</sup>

The discussion thus far suggests that a test with the sign of  $K_{II}$  favoring kinking is less likely to succeed in delivering delamination data than one with the opposite sign of  $K_{II}$ . However, other factors must clearly be in play because some relatively brittle TBC coating systems appear to have a fracture path in the coating just above the interface with the TGO, or just above the bond coat if no TGO is present, due to compressive edge delaminations and buckle delaminations having negative mode II ( $\psi = -90^\circ$ ), or nearly so. These are conditions under which kinking into the coating should be most likely to occur. One possibility is that the thin layer of the coating material just above the interface has significantly lower toughness than the coating itself due to chemical or microstructural differences. Microcracking along, or just above, the interface under thermal exposure, which is thought to produce the degradation of toughness seen in Figs. 3 and 5, would be an example. Another possibility is that the in-plane compressive stress in the coating suppresses any tendency for cracks to wander away from the interface or the low-toughness layer. Quantitative mechanics results are also available to assess the role of residual stress.<sup>23</sup> The relevant dimensionless parameter is

$$\eta = \frac{\sigma\sqrt{c}}{\sqrt{E^*G}} \quad (17)$$

Here,  $\sigma$  is the residual stress,  $c$  is the putative kinked crack length (see Fig. 13), and  $E^* \cong 2(1/\bar{E} + 1/\bar{E}_C)^{-1}$ . A compressive residual stress significantly reduces any tendency to kink into the coating if  $\eta$  is larger in magnitude than about 0.5, and, conversely, a residual tension of this level strongly promotes kinking. Assuming  $c \cong t/10$  and representative values for the other quantities in (17), one concludes that compressive residual stress in the coating can indeed play a role in suppressing kinking even when the sign of  $K_{II}$  favors kinking into the coating.

## V. Conclusions

Experimental measurement of mixed mode delamination toughness as a function of thermal history is an essential element of TBC durability assessment. Edge delaminations are among the most common types of TBC failures, and, therefore, test methods to measure mode II, and near-mode II, delamination toughness must be developed. To date, most toughness data acquired for TBC systems has fallen within the range of mode mix  $0 \leq \psi < 60^\circ$ , using the convention adopted in this paper. Several mixed mode tests have been surveyed here which, in principle, could generate data over the entire range of mode mix, although serious obstacles to their implementation may exist. The compression edge-delamination specimen in Fig. 6 closely mimics edge

delaminations experienced in service, and it may be the most promising test to generate mode II ( $\psi = -90^\circ$ ) toughness data. Friction must be considered in this test, but friction must also be accounted for in any attempt to predict the behavior of an in-service edge delamination. Indeed, friction will have to be considered in any test if contact of the crack faces occurs for mode mixes approaching mode II. Further work to account for the interplay between friction and toughness under near-mode II conditions is needed, especially when the elastic mismatch between the coating and the substrate is large. When the crack is open, the role of the elastic mismatch on the mode mix has been quantified. The shift in mode phase angle is modest as long as the mismatch is not large.

With the conventions adopted in this paper, edge delaminations driven by compressive stress in a coating lying above the substrate experience negative mode II conditions ( $K_{II} < 0$ ,  $\psi = -90^\circ$ ). For this situation, one consequence of negative  $K_{II}$ , as opposed to positive  $K_{II}$ , is the greater tendency for an interface crack to kink out of the interface into the coating interior. This tendency is problematic in any delamination toughness test unless the interface is weak. A residual compressive in the coating helps to counteract the errant propensity. Edge delaminations occurring in service are often observed to be interfacial, or to lie with a layer just above the interface, suggesting that, for whatever the reason, kinking out of the interface plane is suppressed.

## Appendix A

### (A.1) Interfacial Crack Mechanics for General Elastic Mismatch

For a plane strain crack on a planar interface between two isotropic elastic solids, the stresses acting on the interface ( $x_2 = 0$ ) a distance  $r$  ahead of the crack tip within the region dominated by the singular field are<sup>24</sup>

$$\sigma_{22} + i\sigma_{12} = \frac{(K_I + iK_{II})}{\sqrt{2\pi r}} r^{ic} \quad (\text{A-1})$$

with  $i = \sqrt{-1}$  and where

$$\varepsilon = \frac{1}{2\pi} \ln\left(\frac{1-\beta}{1+\beta}\right) \quad (\text{A-2})$$

If  $\beta = 0$ ,  $\varepsilon = 0$  and (A-1) reduces to the usual expression for a homogeneous solid and the mode mix definition in terms of the stresses just ahead of the crack tip is

$$\psi = \tan^{-1}(\sigma_{12}/\sigma_{22}) = \tan^{-1}(K_{II}/K_I)$$

If  $\beta \neq 0$ ,  $\varepsilon \neq 0$  and the crack tip field has an ‘‘oscillatory’’ nature. A number of complications must be considered, including the possibility of crack face interpenetration. In addition, the stress ratio,  $\sigma_{12}/\sigma_{22}$ , from (A-1) is not independent of  $r$  and a specific location on the interface must be identified to define the mode mix.<sup>9,23</sup> Identify a distance  $\ell$  ahead of the crack tip within the zone governed by (A-1) characterizing the fracture process. If the fracture process depends on the relative amount of shear to normal traction on the interface,  $\sigma_{12}/\sigma_{22}$ , then the location  $r = \ell$  is a sensible choice to evaluate the mode mix. With  $r = \ell$  in (A-1),

$$\psi \equiv \tan^{-1}\left(\frac{\sigma_{12}}{\sigma_{22}}\right)_{r=\ell} = \tan^{-1}\left(\frac{\text{Im}((K_I + iK_{II})\ell^{ic})}{\text{Re}((K_I + iK_{II})\ell^{ic})}\right) \quad (\text{A-3})$$

By dimensional considerations, the plane strain solution to any interface crack problem necessarily has the form

$$(K_I + iK_{II}) = \text{Applied stress} \times F \times L^{1/2-ic}$$

where  $F = |F|e^{i\phi}$  is a dimensionless complex function of the

dimensionless parameters in the problem and  $L$  is one of the lengths. By (A-3), it follows that

$$\psi \equiv \tan^{-1}\left(\frac{\sigma_{12}}{\sigma_{22}}\right)_{r=\ell} = \phi + \varepsilon \ln\left(\frac{\ell}{L}\right) \quad (\text{A-4})$$

It is obvious from (A-4) that  $\psi$  depends on the choice of  $\ell$  if  $\varepsilon \neq 0$ . This equation also reveals how the mode mix changes when the choice of  $\ell$  changes. With  $\psi_1$  associated with  $\ell_1$  and  $\psi_2$  associated with  $\ell_2$ , (A-4) gives

$$\psi_2 = \psi_1 + \varepsilon \ln(\ell_2/\ell_1) \quad (\text{A-5})$$

To summarize, when  $\varepsilon \neq 0$ , the mode mix,  $\psi$ , depends on the choice of  $\ell$  and, consequently, the interface toughness  $\Gamma(\psi)$  also implicitly depends on the choice of  $\ell$ . The transformation from one choice to another satisfies

$$\Gamma(\psi_2, \ell_2) = \Gamma(\psi_1 + \varepsilon \ln(\ell_2/\ell_1), \ell_1) \quad (\text{A-6})$$

Illustrations have been given in Hutchinson and Suo.<sup>9</sup>

Some authors have chosen  $\ell$  so as to make the toughness function,  $\Gamma(\psi, \ell)$ , as symmetric as possible with respect to  $\psi$  when fitting data. This is not necessarily the most rational choice of  $\ell$ . It is worth noting that even when  $\beta = 0$  the function  $\Gamma(\psi)$  need not be symmetric in  $\psi$ . Effects contributing to the fracture toughness such as crack tip plasticity and microcracking can produce significant asymmetry in  $\Gamma(\psi)$ .

### (A.2) Beam Theory Solution for Inverted Four-Point Bend Specimen

With reference to the inverted four-point bend specimen in Fig. 6, let  $x$  be measured from the center of the beam and anticipate that an upward force/depth,  $P$ , is exerted by the lower beam on the upper beam at the point of contact just to the right of the center. Further, anticipate that there is no other contact between the beams in the interval  $0 < x < a$ . At  $x = 0$ , the lower beam has moment  $M$  while the upper beam sustains no moment. At  $x = a$ , the deflections and the slopes of the two beams must coincide. Under these assumptions,  $P = 3M/(4a)$  and the difference between the deflections of the vertical deflections of the upper and lower beams is found to be

$$w_{\text{upper}} - w_{\text{lower}} = \frac{1}{4} \frac{Ma^2}{B} \frac{x}{a} \left(1 - \frac{x}{a}\right)^2$$

in accord with starting assumption. The energy release rate can be computed directly by the derivative of the total energy with respect to  $a$  giving (7). In addition, as  $x \rightarrow a$ , one finds  $M_{\text{upper}} = 3M/4$  and  $M_{\text{lower}} = M/4$ . The mode mix,  $\psi = -60^\circ$ , can be estimated using the exact results<sup>9</sup> for a infinite layer with a semi-infinite crack such that the equal thickness layers above and below the crack support moments  $M_{\text{upper}} = 3M/4$  and  $M_{\text{lower}} = M/4$ , respectively, and the uncracked layer to the right supports  $M$ . It can also be noted that the energy release for this exact solution agrees with the direct calculation based on the beam solution in (7).

### (A.3) Finite Element Modeling

ANSYS version 12.1 was used for the linear-elastic finite element modeling of the inverted four-point bend specimen and the compression edge-delamination specimen.<sup>11</sup> The general modeling approach was as follows: (i) the specimen geometry and loading was parameterized; and (ii) a customized ANSYS script was written to preprocess, solve, and postprocess the static solution for each specimen crack length independently, i.e., crack growth was not explicitly modeled.

Specimens dimensions were selected to ensure fairly slender layers, e.g.,  $L/h = 20$  and  $a/L \leq 2$  where  $a$  is the crack half-length emerging from the ‘‘small’’ notch with half-width  $b = h/10$  in the

<sup>11</sup>ANSYS v12.1 Mechanical & Mechanical APDL Documentation.

center of the top layer, and  $L$  is the total half-length (parallel to the crack) of the specimen. The inverted four-point bend specimen was subjected to a linear longitudinal stress distribution remote from the crack tip defined to give a “pure” bending moment  $M$  as shown in Fig. 6. The compression edge-delamination specimen was subjected to a prescribed, uniform longitudinal compressive displacement generated by the rigid platens depicted in Fig. 6. The load  $P$  was given by the sum of the corresponding axial nodal reactions.

Relatively coarse meshes comprised of plane-strain 2D, quadratic eight-node elements were used away from the crack tip, e.g., 32 elements through the total specimen thickness. Singular forms of these elements, wherein the mid-side nodes are placed at the quarter points to produce an asymptotic square-root stress/strain singularity, were used to mesh the first row of elements defining the crack tip such that the maximum element edge length did not exceed 2.5% of  $h$ . Relatively fine meshes were used to transition between the coarsely meshed regions and the crack tip, e.g., 200 quadrilaterals in the axial and transverse directions for a bounding box with a maximum (total) edge length of about one-quarter  $h$ ; and a small number of quadratic six-node elements comprised the perimeter of this transitional region—well away from the crack tip as these are not permitted in the  $J$ -integral calculation mentioned below. At the crack faces, the initial coarse mesh was refined (e.g., initial edge length divided by four) using a combination of six-node and eight-node quadratic elements; then, three-node quadratic contact (a.k.a. slave) and target (a.k.a. master) elements were overlaid on the free faces of the existing elements comprising the crack faces.

Crack face contact was modeled using standard, unilateral contact along the entire crack length such that the crack faces could open, or separate, via a transverse (normal to the crack faces) displacement gap between the contact/target elements; or, the crack faces could close such that a nonzero contact pressure developed. Most of the default ANSYS standard-contact options were selected such that contact interference was minimized using an augmented Lagrangian approach with automatic solution control. Coulomb friction was specified with a coefficient of friction  $\mu_f$ . Note that, because the crack faces were treated as initially co-linear (e.g., essentially zero initial gap to within numerical tolerances), the contact problem is one involving closely conforming surfaces such that, in general, many nonlinear Newton–Raphson iterations are required to solve for the crack-face contact pressure and contact gap distributions; the number of iterations needed increases with  $\mu_f$ .

Once the static solution was obtained for each specimen crack length, the energy release rate was calculated using ANSYS’  $J$ -integral, the mode mix was determined using ANSYS’ interaction integrals for the stress intensity factors. For comparison purposes, this result was checked via ANSYS’ more approximate crack-tip displacement extrapolation for the stress intensity factors. In the range of crack lengths considered, the crack tip was closed and the mode II stress intensity was negative. Corresponding mode I stress intensities were positive for the inverted four-point bend specimen, whereas small-magnitude (i.e., up to about 10% of mode II) negative mode I stress intensities were calculated for the compression edge-delamination specimen. The latter result is probably due to the numerically approximate enforcement of the ideal point-wise penetration constraint. One would expect zero mode I if this constraint was perfectly satisfied.

For ease of postprocessing, only “average” contact pressure and contact gap data were tabulated, i.e., nodal pressures/gaps averaged at the centroid of each contact element. This is acceptable because these data are only used to gain qualitative insight into the effects of crack face contact. In addition, the contact element mesh is apparently not overly coarse given the relatively “smooth” appearance of much these data when plotted. However, for “small”  $a/h$ , e.g.,  $a/h = 0.4$  in Fig. 11(A), one expects the (elastic) contact pressure distribution to be

asymptotically singular as  $x/a \rightarrow 1$  because of the “effective” reentrant corner formed at the (transverse) notch contact when closed; this detail is not captured here, nor do we anticipate a significant error in the crack-tip quantities calculated as a result of this approximation. The singular pressure behavior also shows up in the limit of  $x/a \rightarrow 1$  for the inverted four-point bend specimen.

## Acknowledgments

The authors are indebted to M. R. Begley, G. Ojard, G.V. Srinivasan, and F. Zok for helpful discussions.

## References

- <sup>1</sup>N. P. Padture, M. Gell, and E. H. Jordan, “Thermal-Barrier Coatings for Gas-Turbine Engine Applications,” *Science*, **296**, 280–4 (2002).
- <sup>2</sup>D. R. Clarke and C. G. Levi, “Materials Design for the Next Generation Thermal-Barrier Coatings,” *Annu. Rev. Mater. Res.*, **33**, 383–417 (2003).
- <sup>3</sup>A. G. Evans, D. R. Mumm, J. W. Hutchinson, G. H. Meier, and F. S. Pettit, “Mechanisms Controlling the Durability of Thermal-Barrier Coatings,” *Prog. Mater. Sci.*, **46**, 505–53 (2001).
- <sup>4</sup>S. Kraemer, S. Faulhaber, M. Chambers, D. R. Clarke, C. G. Levi, J. W. Hutchinson, and A. G. Evans, “Mechanisms of Cracking and Delaminations within Thick Thermal Barrier Systems in Aero-Engines Subject to Calcium–Magnesium–Alumino–Silicate (CMAS) Penetration,” *Mater. Sci. Eng. A*, **490**, 26–35 (2008).
- <sup>5</sup>I. Hofinger, M. Oechsner, H.-A. Bahr, and M. V. Swain, “Modified Four-Point Bend Specimen for Determining the Interface Fracture Energy for Thin, Brittle Layers,” *Int. J. Fracture*, **92**, 213–20 (1998).
- <sup>6</sup>P.-Y. Thery, M. Poulain, M. Dupeux, and M. Braccini, “Spallation of Two Thermal Barrier Coating Systems: Experimental Study of Adhesion and Energetic Approach to Lifetime During Cyclic Oxidation,” *J. Mater. Sci.*, **44**, 1726–33 (2009).
- <sup>7</sup>H. H. Yu, M. Y. He, and J. W. Hutchinson, “Edge Effects in Thin Film Delamination,” *Acta Mater.*, **49**, 93–107 (2001).
- <sup>8</sup>D. Balint and J. W. Hutchinson, “Mode II Edge Delamination of Compressed Thin Films,” *J. Appl. Mech.*, **68**, 725–30 (2001).
- <sup>9</sup>J. W. Hutchinson and Z. Suo, “Mixed Mode Cracking in Layered Materials,” *Adv. Appl. Mech.*, **29**, 63–191 (1992).
- <sup>10</sup>A. Vastinonta and J. L. Beuth, “Measurement of Interfacial Toughness in Thermal Barrier Coating Systems by Indentation,” *Eng. Fract. Mech.*, **68**, 843–60 (2001).
- <sup>11</sup>C. Eberl, D. S. Gianola, Xi Wang, M. Y. He, A. G. Evans, and K. J. Hemker, “In Situ Measurement of the Toughness of the Interface Between a Thermal Barrier Coating and a Ni Alloy,” *J. Am. Ceram. Soc.* (this issue).
- <sup>12</sup>S. Q. Guo, D. R. Mumm, A. M. Karlsson, and Y. Kagawa, “Measurement of Interfacial Shear Mechanical Properties in Thermal Barrier Coating Systems by a Barb Pullout Method,” *Ser. Mater.*, **53**, 1043–8 (2005).
- <sup>13</sup>M. Tanaka, Y. F. Liu, S. S. Kim, and Y. Kagawa, “Delamination Toughness of Electron Beam Physical Vapor Deposition (EB-PVD) Y2O3–ZrO2 Thermal Barrier Coatings by the Pushout Method: Effect of Thermal Cycling Temperature,” *J. Mater. Res.*, **23**, 2382–92 (2008).
- <sup>14</sup>Y. F. Liu, Y. Kagawa, and A. G. Evans, “Analysis of a “Barb Test” for Measuring the Mixed-Mode Delamination Toughness of Coatings,” *Acta Mater.*, **56**, 43–9 (2008).
- <sup>15</sup>P. G. Charalambides, J. Lund, A. G. Evans, and R. M. McMeeking, “A Test Specimen for Determining the Fracture Resistance of Bimaterial Interfaces,” *J. Appl. Mech.*, **56**, 77–82 (1989).
- <sup>16</sup>G. Bao, S. Ho, B. Fan, and Z. Suo, “The Role of Material Orthotropy in Fracture Specimens for Composites,” *Int. J. Solids Struct.*, **29**, 1105–16 (1992).
- <sup>17</sup>B. F. Sorensen, K. Jorgensen, T. Jacobsen, and R. C. Ostergaard, “DCB-Specimen with Uneven Bending Moments,” *Int. J. Fracture*, **141**, 163–76 (2006).
- <sup>18</sup>J. S. Wang and Z. Suo, “Experimental Determination of Interfacial Toughness Curves Using Brazil-Nut-Sandwiches,” *Acta Metall.*, **38**, 1279–90 (1990).
- <sup>19</sup>L. Bank-Sills, V. Boniface, and R. Eliasi, “Development of a Methodology for Determination of Interface Fracture Toughness of Laminate Composites—the 0°/90° Pair,” *Int. J. Solids Struct.*, **42**, 663–89 (2005).
- <sup>20</sup>A. Dorogoy and L. Banks-Sills, “Effective of Crack Face Contact and Friction on Brazilian Disk Specimens—A Finite Difference Solution,” *Eng. Fract. Mech.*, **72**, 2758–73 (2005).
- <sup>21</sup>Z. Suo and J. W. Hutchinson, “Sandwich Test Specimens for Measuring Interface Crack Toughness,” *Mater. Sci. Eng.*, **A107**, 135–43 (1989).
- <sup>22</sup>K. M. Liechti and Y.-S. Chai, “Asymmetric Shielding in Interfacial Fracture Under Inplane Shear,” *J. Appl. Mech.*, **59**, 295–304 (1992).
- <sup>23</sup>M. Y. He, A. Bartlett, A. G. Evans, and J. W. Hutchinson, “Kinking of a Crack Out of an Interface: Role of In-Plane Stress,” *J. Am. Ceram. Soc.*, **74**, 767–71 (1991).
- <sup>24</sup>J. R. Rice, “Elastic Fracture Concepts for Interfacial Cracks,” *J. Appl. Mech.*, **55**, 98–103 (1988).